

# Orders of Magnitude Improvement in Coherence of Silicon-Vacancy Ensembles in Isotopically Purified 4H-SiC

I. Lekavicius<sup>1,\*</sup>, R.L. Myers-Ward,<sup>2</sup> D.J. Pennachio<sup>1</sup>, J.R. Hajzus<sup>1</sup>, D.K. Gaskill,<sup>2,†</sup> A.P. Purdy,<sup>2</sup> A.L. Yeats,<sup>2</sup> P.G. Brereton<sup>1</sup>,<sup>‡</sup> E.R. Glaser,<sup>2</sup> T.L. Reinecke,<sup>2</sup> and S.G. Carter<sup>1,2,†</sup>

<sup>1</sup> NRC Research Associate at the US Naval Research Laboratory, Washington, DC 20375, USA

<sup>2</sup> US Naval Research Laboratory, Washington, DC 20375, USA

<sup>3</sup> ASEE Research Associate at the US Naval Research Laboratory, Washington, DC 20375, USA

<sup>4</sup> US Naval Academy, Annapolis, Maryland 21402, USA



(Received 31 August 2021; accepted 18 February 2022; published 16 March 2022)

For solid-state spin systems, unwanted interactions with surrounding spin baths and inhomogeneity are ubiquitous challenges. In defect spin systems, part of this challenge is that the process of generating the desired defect often involves creating numerous unwanted defects that induce dephasing. Here we show that many of these issues can be alleviated with the silicon vacancy in silicon carbide (SiC), which is a simple defect to produce as it does not require the introduction of impurity atoms into the crystal. Previous measurements of the inhomogeneous dephasing time  $T_2^*$  of silicon-vacancy ensembles have thus far been limited to a few 100 ns due to the nuclear spin bath. We perform isotopic purification to minimize the influence of nuclear spins, leading to an order of magnitude improvement in the  $T_2^*$  at room temperature. Further improvements emerge by suppressing the effects of strain inhomogeneity via an informed choice of basis in the spin quartet. Combining these techniques leads to about a factor 50 improvement in the  $T_2^*$  of the defect ensemble even at high defect densities.

DOI: 10.1103/PRXQuantum.3.010343

## I. INTRODUCTION

Coherence properties of quantum systems are the key features that allow them to operate nonclassically and to outperform their classical counterparts in applications ranging from sensing, communications, and computation. As such, it is an ever present technical challenge to achieve long coherence times by isolating quantum systems from unwanted environmental interactions. Systems of trapped ions and atoms are intrinsically isolated from these interactions and therefore exhibit some of the longest coherence times measured to date [1,2]. However, these systems often have limited real-world applications due to the high levels of technical overhead needed to implement them. Defects in solid-state systems offer an attractive alternative, as they

possess atomlike energy-level structures within the band gap of the solid while being essentially fixed at a location in the lattice.

One of the most ubiquitous solid-state defects is the nitrogen-vacancy (NV) center in diamond. The success of this system is due to its impressive spin properties at room temperature, chief among them being its robust spin ground-state coherence, optical initialization, and readout [3,4]. These properties, which allow for the utilization of the NV center as a quantum sensor in ambient conditions, have led to the development of NV-based magnetometers. The combination of high sensitivity and high spatial resolution of the NV magnetometer has led to numerous advancements and applications, ranging from the imaging of magnetic textures in condensed-matter systems [5] to neuron action potentials [6]. However, the diamond NV system has a number of disadvantages, such as the price and difficulty of fabrication involved with the host crystal. In addition, the required introduction of nitrogen to the carbon host crystal, typically at much higher concentrations than the desired NV center, often results in a significant electronic spin bath [7], which causes decoherence of the NV ensemble and requires spin-bath driving [8] to suppress. As such, alternative systems to this platform are being investigated [9]. A prime candidate for room-temperature quantum sensing is the silicon-vacancy

\*ilekavicius91@gmail.com

†sam.carter@nrl.navy.mil

<sup>‡</sup>Current affiliation: Institute for Research in Electronics and Applied Physics, University of Maryland, College Park, Maryland, 20742, USA.

Published by the American Physical Society under the terms of the [Creative Commons Attribution 4.0 International license](#). Further distribution of this work must maintain attribution to the author(s) and the published article's title, journal citation, and DOI.

center in 4H-SiC [10–16], which has been shown to possess similar room-temperature spin initialization and readout properties [17,18] as well as a reasonably long-lived ground-state coherence [19–21].

In the 4H-SiC polytype, the silicon vacancy can be located in two nonequivalent sites in the lattice. In this work, we focus exclusively on the V2 center, which is negatively charged, possesses a  $S = 3/2$  ground state, emits a zero-phonon line at 916 nm and, unlike the V1 center, has had optically detected magnetic resonance (ODMR) spectra observed at room temperature [17]. The ground-state Hamiltonian of the V2 center is given as

$$H = DS_z^2 + g\mu_B \vec{B} \cdot \vec{S} + H_{\text{hf}} + H_{\text{ES}} + \Xi \sum_{\alpha\beta} u_{\alpha\beta} S_\alpha S_\beta, \quad (1)$$

where  $\vec{S} = (S_x, S_y, S_z)$  is the spin-3/2 operator,  $g$  is the V2 center electronic  $g$  factor,  $\mu_B$  is the Bohr magneton,  $H_{\text{hf}}$  is the hyperfine Hamiltonian,  $H_{\text{ES}}$  is the electronic spin Hamiltonian,  $\Xi$  is the ground-state deformation potential under the spherical approximation [22],  $u_{\alpha\beta}$  is the strain tensor and  $2D = 70$  MHz is the zero field splitting (ZFS) between the  $|\pm 3/2\rangle$  and  $|\pm 1/2\rangle$  states [Fig. 1(a)]. The hyperfine Hamiltonian describes the coupling of the V2 center with the nuclear bath spins surrounding it, resulting in a time-varying magnetic field which causes dephasing between the different spin states. The electronic spin coupling can likewise cause dephasing due to spin-spin interactions between the V2 center and other electronic spins (including other V2 centers in the ensemble), while the primary effect of the strain coupling is to shift the ZFS parameter by an amount  $\delta D = \Xi (u_{\text{para}} - u_{\text{perp}})$ , where  $u_{\text{para(perp)}}$  is the on-axis (off-axis) strain experienced by the defect. Inhomogeneity in the strain environment within an ensemble leads to spin dephasing between spin states separated by the ZFS.

Off-resonant optical excitation of the center polarizes the defect into a subset of its quartet ground state while also providing state-dependent photoluminescence via a spin-dependent intersystem crossing [23–25]. These two features are key in realizing a room-temperature magnetometry scheme. In addition, the quartet structure possesses a ground-state-level anticrossing at moderate magnetic fields, which allows for rf-free magnetometry schemes [15,16]. The spin coherence time is also of great importance, and there have been a number of investigations of ensembles of silicon-vacancy centers [20,21,26,27] and even single centers [19,28]. For ensembles of V2 centers, previous experiments referenced above show inhomogeneous dephasing times  $T_2^* = 200$ –300 ns, Hahn echo decay times  $T_2 = \sim 50$   $\mu$ s, and room-temperature spin-lattice relaxation times  $T_1 = 340$   $\mu$ s. While echo-pulse sequences can be used to extend spin coherence to much longer times than  $T_2^*$ , these sequences limit sensing to high frequencies above  $1/T_2$ . For low frequency or dc sensing, the sensitivity is limited by  $T_2^*$ , which has thus far been relatively short for V2 ensembles.

In the extensive body of work done with NV magnetometry [29], significant improvements of both single and ensemble NV-center dephasing times resulted from isotopic purification of the diamond lattice ( $^{13}\text{C} = 1.1\%$ ). It is then reasonable to expect the dominant dephasing mechanism in natural isotopic abundance 4H-SiC is the nuclear spin bath of the lattice ( $^{29}\text{Si} = 4.7\%$ ,  $^{13}\text{C} = 1.1\%$ ), which possess a denser concentration of nuclear-spin-carrying isotopes than diamond. This has motivated various investigations of the effects of decreased nuclear spin density [30] on the coherence of both divacancy [31,32] and silicon-vacancy [16] defects in SiC, though there is comparatively little work done with silicon-vacancy ensembles in high isotopic purity material [27]. In this work, we report on large improvements to the room temperature  $T_2^*$  of V2 ensembles by growing isotopically purified (isopure) 4H-SiC epilayers ( $^{13}\text{C} = 0.15\%$  and  $^{29}\text{Si} = 0.01\%$ ), to

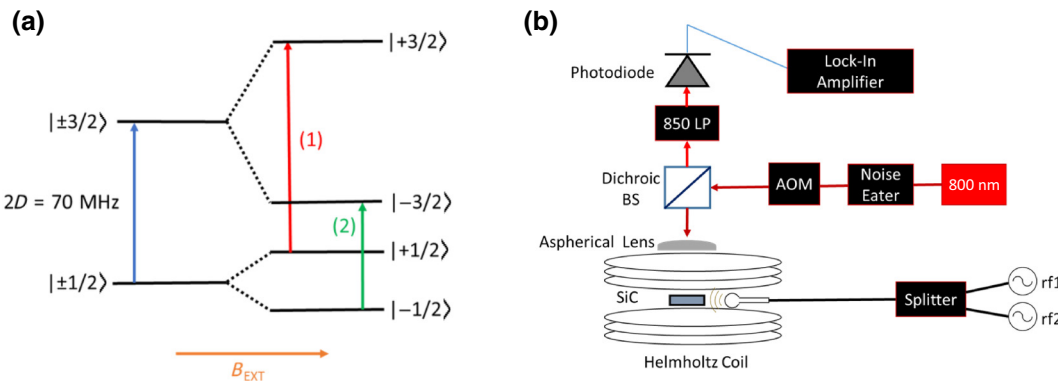


FIG. 1. V2 ground state and experiment setup. (a) Energy-level structure of V2 center with an external magnetic field oriented along the  $c$ -axis splitting the degeneracy of the  $|\pm 1/2\rangle$  and  $|\pm 3/2\rangle$  states. (b) Experimental setup for measurement of V2 ODMR.

minimize isotopes with nuclear spins. The grown isopure epilayer and a reference epilayer with natural isotope abundance are irradiated with electrons at 1 MeV and at varying doses to produce silicon vacancies. We obtain roughly an order of magnitude improvement in  $T_2^*$  for the isotopically purified sample when measuring in the  $m_s = \{1/2, 3/2\}$  basis, with  $T_2^*$  decreasing as the irradiation dose increases. We attribute much of this dose dependence to strain inhomogeneity based on complementary measurements in the  $m_s = \{-1/2, 1/2\}$  basis, which is largely immune to strain and temperature fluctuations [27]. In this basis  $T_2^*$  is significantly longer and has only a weak dependence on irradiation dose. Annealing at temperatures up to 700 °C results in modest improvements, giving a  $T_2^*$  on the order of 20  $\mu$ s in the  $m_s = \{-1/2, 1/2\}$  basis. These results pave the way for room-temperature sensing applications using high-density ensembles of silicon vacancies with long spin-dephasing times.

## II. SUPPRESSION OF NUCLEAR SPIN-INDUCED DEPHASING

A diagram of the experimental setup for ODMR is given in Fig. 1(b). A series of continuous-wave ODMR scans at varying external magnetic fields obtained for a natural isotope abundance V2 ensemble sample are shown in Fig. 2(a). The spin-dependent intersystem crossing results in differing nonradiative relaxation rates between the two spin subsets, allowing for off-resonant optical polarization and measurement of the population difference between  $|\pm 1/2\rangle$  and  $|\pm 3/2\rangle$ . The most intense ODMR signals occur from the  $|1/2\rangle$  to  $|3/2\rangle$  and  $|-1/2\rangle$  to  $|-3/2\rangle$  transitions. The  $|1/2\rangle$  to  $|-1/2\rangle$  transition is allowed but does not typically appear in ODMR as this transition does not change the relative populations between the  $|\pm 3/2\rangle$  and  $|\pm 1/2\rangle$  sublevels. Due to state mixing from strain and off-axis magnetic fields, normally dipole forbidden  $\Delta m_s = 2$  transitions are also visible, albeit at significantly lower intensities. A typical ODMR spectrum of the  $|1/2\rangle \rightarrow |3/2\rangle$  transition at a fixed external magnetic field (11 mT) is shown in Fig. 2(b). Here we note the commonly observed side peaks of V2 centers due to next-nearest-neighbor  $^{29}\text{Si}$  hyperfine coupling [33]. The ODMR spectrum for an isopure SiC sample in Fig. 2(c) shows no hyperfine side peaks, confirming the removal of the majority of  $^{29}\text{Si}$  isotopes. The isopure sample also shows a narrower linewidth than the natural abundance sample for an equivalent power broadening, suggesting an improvement in dephasing time.

Ramsey interferometry is performed on these samples to quantify the inhomogeneous dephasing time  $T_2^*$ . An 800-nm laser is pulsed for 3  $\mu$ s to initialize the V2 center ground state [Fig. 3(a)]. A  $\pi/2$  rf pulse, resonant with the  $|1/2\rangle \rightarrow |3/2\rangle$  transition, creates an evenly weighted superposition of the two states. The superposition is then

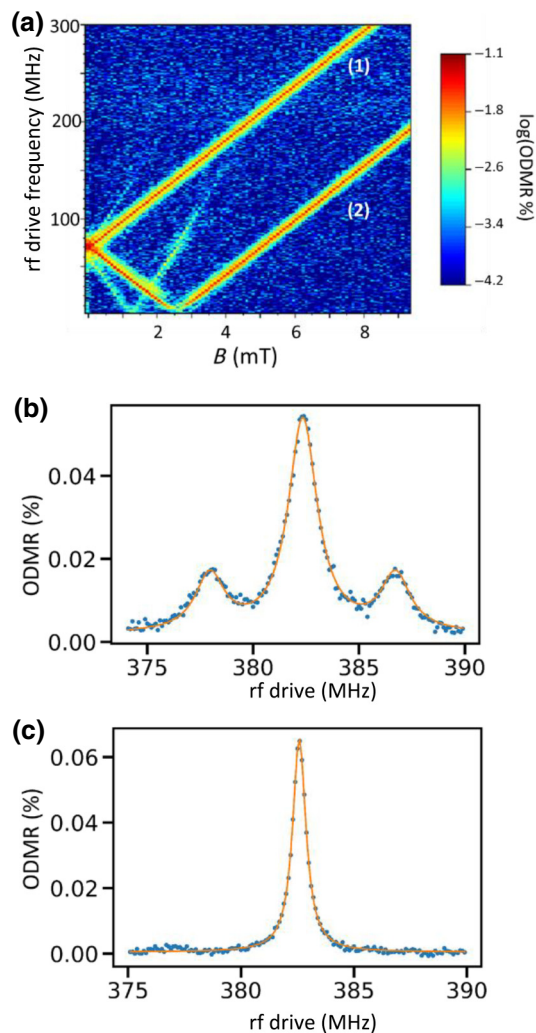


FIG. 2. V2 optically detected magnetic resonance. (a) Ground-state ODMR map as a function of external magnetic field and rf drive frequency. Transitions (1) and (2) correspond to those labeled in Fig. 1(a). The overall PL signal of the lock-in amplifier is 1.2 V, with a maximum ODMR signal of 0.08% represented on the color scale. This scan was performed with relatively low rf power. (b) Single ODMR scan on a natural isotope abundance sample at  $B = 11$  mT. The presence of hyperfine-coupling-detuned side peaks is due to next-nearest-neighbor  $^{29}\text{Si}$  isotopes (dose =  $3 \times 10^{18} \text{ cm}^{-2}$ ). The rf power is  $-5$  dBm going to a shorted coax loop antenna (leading to approximately 200 kHz Rabi frequency). Three Lorentzian fits are shown, all with an equivalent FWHM of 1.6 MHz. (c) ODMR scan on an isopure SiC sample with the same irradiation parameters as (b) as well as equivalent rf drive power. A single Lorentzian fit is plotted, showing a FWHM of 0.71 MHz.

left to precess and decay for a variable time before a second  $\pi/2$  pulse projects the superposition onto a population difference between  $|1/2\rangle$  and  $|3/2\rangle$ , dependent on the phase accumulated during the free precession. The Ramsey pulse experiment characterizes the static inhomogeneities and low-frequency, primarily magnetic, noise the

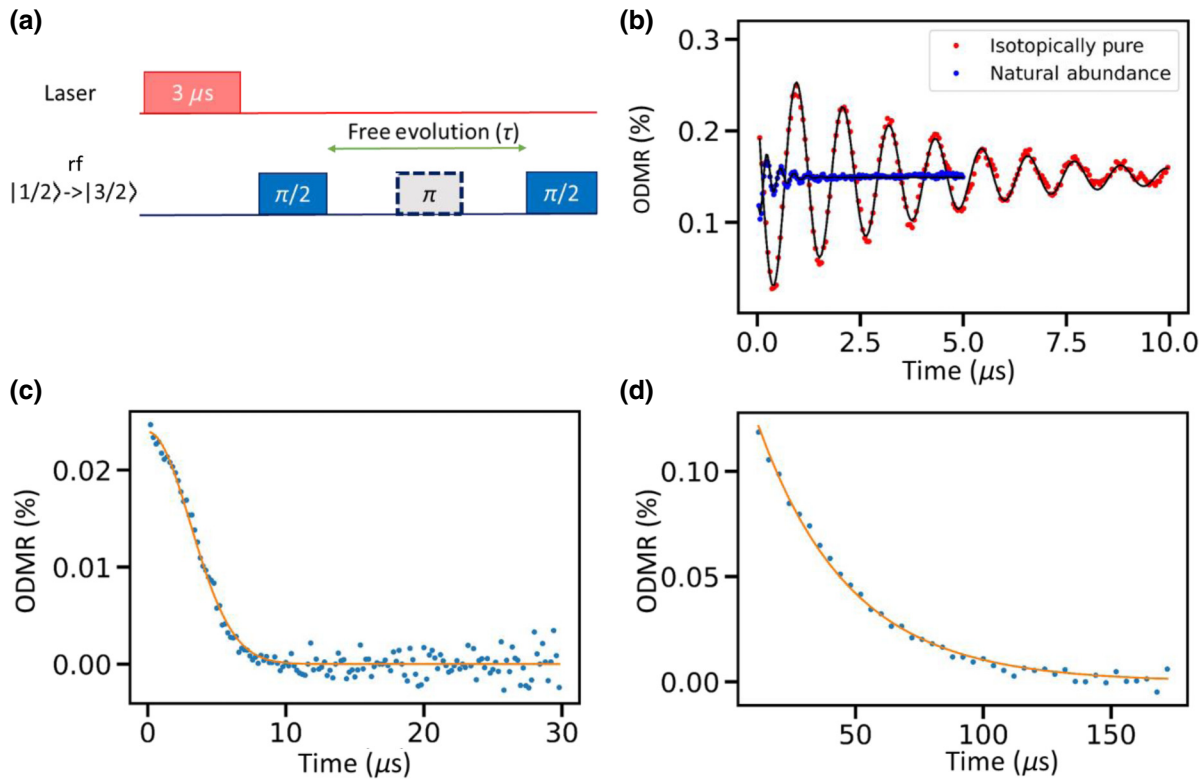


FIG. 3. Ramsey and Hahn echo on the V2 ensemble. (a) Pulse sequence for Ramsey scheme and Hahn echo scheme ( $\pi$  pulse in dashed box). The  $\pi/2$  pulse length for the natural abundance sample is 120 ns, while the pulse length for the isopure sample is 400 ns. (b) Ramsey fringe comparison at 11 mT between isopure and natural abundance samples of the same irradiation dose ( $3 \times 10^{17} \text{ cm}^{-2}$ ), with fit  $T_2^*$  of 4  $\mu\text{s}$  and 400 ns, respectively. Both are fit to  $A \sin(2\pi ft + \varphi) \exp(-t/T_2^*) + B$  (plotted in black). The signal contrast for the natural abundance sample is lower due to the far off-resonant drive of the rf pulses. (c) Hahn echo decay of the V2 ensemble (blue dots) in natural abundance sample ( $3 \times 10^{18} \text{ cm}^{-2}$ ) at approximately 4 mT. The  $T_2$  is given as 4.3  $\mu\text{s}$  from a Gaussian fit  $A \exp[-(t/T_2)^2]$  (orange line). Unlike the Ramsey interferometry, the Hahn echo of the natural abundance sample is done with the rf near resonance ( $\pi/2$  pulse length of 400 ns). (d) Hahn echo of the V2 ensemble in the isopure sample at the same irradiation dose and magnetic field as in (c).  $T_2$  is given as 35.7  $\mu\text{s}$  from an exponential fit  $A \exp(-t/T_2)$ .

ensemble of V2 centers experiences. Ramsey interferometry data for a reference sample and isopure sample, both irradiated at  $3 \times 10^{17} \text{ cm}^{-2}$ , are given in Fig. 3(b). The oscillation frequency of the Ramsey fringes is equal to the detuning of the rf pulse from the driven transitions. For better fitting of the decoherence time, this detuning is chosen to allow at least a few periods before the Ramsey fringes fully decay. The reference sample has an exponential decay time  $T_2^* = 400 \text{ ns}$ , consistent with results from other ensemble studies in natural abundance 4H-SiC [21], and a frequency of 3 MHz due to the far detuned rf pulse. The isopure sample shows a much longer  $T_2^* = 4 \text{ } \mu\text{s}$ , with an oscillation frequency of approximately 900 kHz. This smaller detuning of 900 kHz is used in the isopure case due to the longer-lived signal. The order of magnitude improvement confirms that the dominant inhomogeneous dephasing mechanism in the natural abundance sample is the variation in the nuclear spin environment.

In addition, we measure the Hahn echo decay time,  $T_2$ , which characterizes the high-frequency magnetic noise in

the system and is a key parameter in ac magnetic field sensing [29]. In this case, an additional rf  $\pi$  pulse [dashed line in Fig. 3(a)] is placed between the two  $\pi/2$  pulses, reversing any dephasing due to slow or static variations to form an echo at the second  $\pi/2$  pulse. Figure 3(c) shows a Hahn echo decay curve for a natural abundance sample irradiated at  $3 \times 10^{18} \text{ cm}^{-2}$ , with a Gaussian decay time  $T_2 = 4.3 \text{ } \mu\text{s}$ . This data is taken at low magnetic field (approximately 4 mT), resulting in a fast decay rate induced by electronic spin-echo envelope modulation from interaction with the nuclear spin bath [21]. In contrast, the Hahn echo decay of the isopure sample at the same irradiation dose [Fig. 3(d)] gives an exponential decay time  $T_2 = 35.7 \text{ } \mu\text{s}$ . The difference in both magnitude of  $T_2$  as well as the shape of the fit suggests that the density of the decoherence source has transitioned to the dilute regime, evidenced by the transition of the Hahn echo from a Gaussian to an exponential decay [34].

In Fig. 4, the  $T_2^*$  and  $T_2$  values in the  $m_s = \{1/2, 3/2\}$  basis are compared across the four different electron

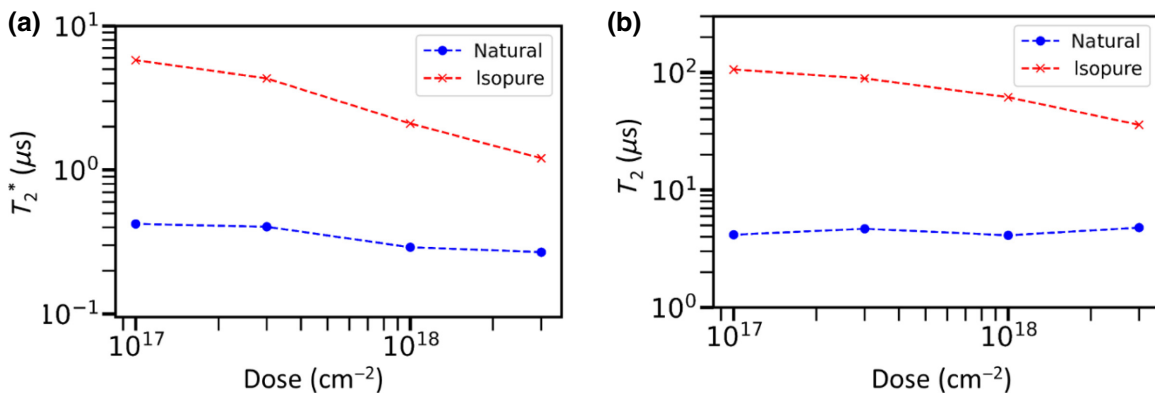


FIG. 4. Dose dependence of  $T_2^*$  and  $T_2$  in  $m_s = \{1/2, 3/2\}$  basis. (a) Inhomogeneous dephasing time  $T_2^*$  versus irradiation dose for all eight samples. (b) Hahn echo decay time  $T_2$  for all eight samples.

irradiation doses spanning 1.5 orders of magnitude for both isopure and natural abundance samples. Figure 4(a) shows that the  $T_2^*$  for the reference samples display weak dependence on the dose, indicating that dephasing is dominated by magnetic noise in its nuclear spin environment. Conversely, the isopure samples show a stronger decrease in  $T_2^*$  with increasing irradiation dose. The dose dependence of the Hahn echo decay time  $T_2$  follows a similar pattern [Fig. 4(b)]. For the isopure samples, the optimal coherence times occur for the lowest dose sample ( $1 \times 10^{17} \text{ cm}^{-2}$ ), resulting in a  $T_2^* = 5.7 \mu\text{s}$  and a  $T_2 = 105 \mu\text{s}$ . Although this strong dose dependence suggests that dipole-dipole interactions with irradiation-induced defects are the limiting factors in the  $T_2$  coherence times [29], we show this is not the case for  $T_2^*$ .

### III. SUPPRESSION OF STRAIN-INDUCED DEPHASING

With nuclear spin noise largely suppressed, we can investigate other noise sources whose effects were previously negligible to the overall dephasing rate of the V2 ensemble. Strain inhomogeneities are a common source of decoherence in ensemble solid-state defect systems, as static strain can cause a shift in the ZFS of the spin ground state. The effects of this decoherence can be mitigated by working in a basis with states whose energy differences are not dependent on the ZFS, which has been demonstrated for the NV in diamond by working in the double quantum  $\{-1, +1\}$  basis [8,35–37]. Working in the V2 center  $\{-1/2, 1/2\}$  basis provides this benefit but adds some technical complexity as there is no PL intensity difference between these two states as there is between the  $\{1/2, 3/2\}$  states. In addition this is a single quantum basis, meaning that the transition can be directly driven with rf fields and that modified Ramsey pulse sequences will not be necessary to cancel out the residual single quantum signal from the double quantum signal as in the case of the NV [37].

A modified Ramsey pulse sequence is used to characterize  $T_2^*$  in the  $\{-1/2, 1/2\}$  basis [Fig. 5(a)]. First, a 3- $\mu\text{s}$  laser pulse initializes the spin state of the V2 ensemble. Next, an initial  $\pi$  pulse inverts the population between  $|1/2\rangle$  and  $|3/2\rangle$ , after which a second rf source performs the standard Ramsey pulse sequence between  $|1/2\rangle$  and  $| -1/2\rangle$ . A final  $\pi$  pulse then inverts the  $|1/2\rangle$  and  $|3/2\rangle$  population, projecting the population difference between the  $|\pm 1/2\rangle$  states into the  $\{-1/2, 3/2\}$  basis, which is then measured by the 3- $\mu\text{s}$  laser pulse of the next sequence. For this scheme, the shorted coaxial antenna is replaced with a printed circuit board coplanar waveguide due to its more uniform rf field amplitude. Figure 5(b) shows a Ramsey fringe comparison in the two different bases for the isopure sample irradiated at  $3 \times 10^{18} \text{ cm}^{-2}$ . This measurement is done at very low external magnetic field (approximately 0.3 mT) due to current noise in the Helmholtz coil that significantly contributes to the dephasing rate in the  $\{-1/2, 1/2\}$  basis measurement. The suppression of the strain inhomogeneity in this new basis leads to a drastic increase of the  $T_2^*$  from  $1.2 \mu\text{s}$  to  $13.7 \mu\text{s}$ . The magnitude of this increase suggests that inhomogeneity in the zero field splitting (most probably caused by irradiation-induced strain), not defect spin density, is the primary mechanism behind the dose-dependent decoherence rates observed in Fig. 4(a). The loss of relative contrast in the  $\{-1/2, 1/2\}$  basis is due in large part to imperfect inversion from long  $\pi$  pulse lengths (comparable to  $T_2^*$  in the  $\{1/2, 3/2\}$  basis), and can be mitigated by using higher power rf sources and amplifiers.

Attempting to alleviate this strain, the samples are annealed at various temperatures in atmospheric conditions for 2 h. The  $T_2^*$  in both bases for the highest dose isopure sample is shown in Fig. 5(c) as a function of annealing temperature. A clear improvement in  $T_2^*$  is seen as the annealing temperature increases, the highest of which results in nearly a factor of 2 increase in the  $\{1/2, 3/2\}$  basis at 700 °C. Surprisingly, an increase

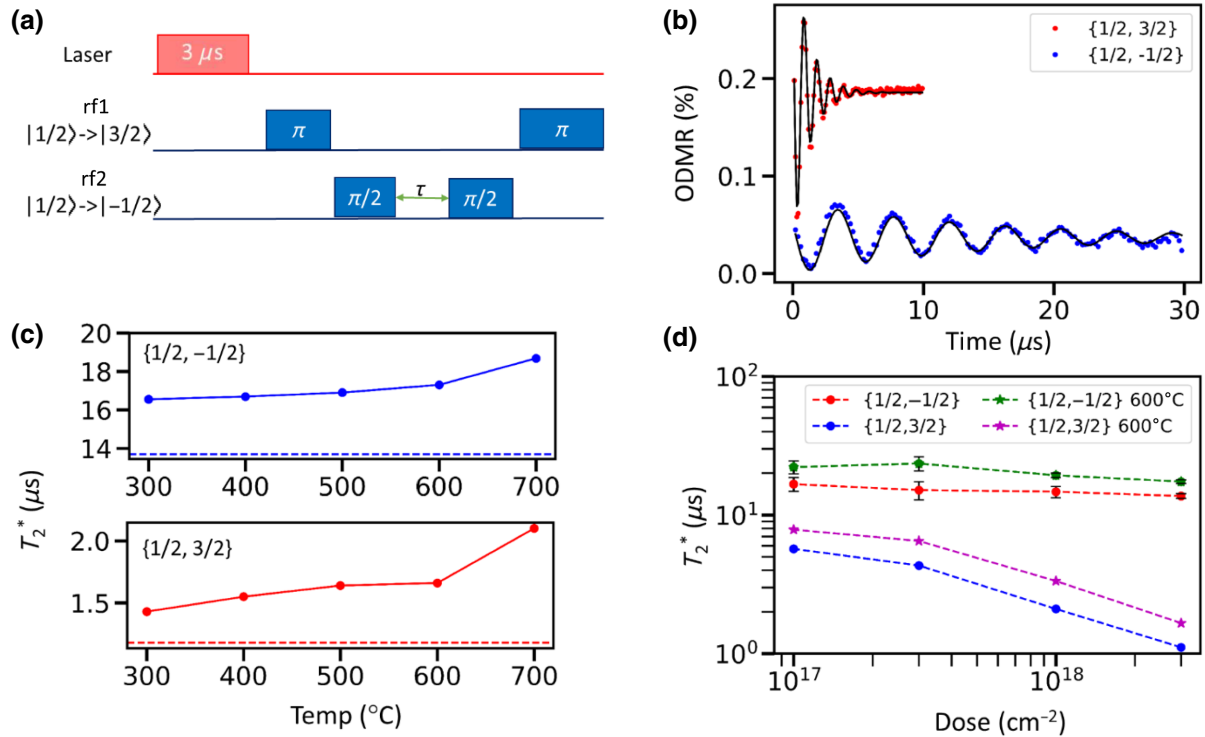


FIG. 5. Suppression of strain-induced dephasing. (a) rf and optical pulse sequence for Ramsey interferometry in the  $\{1/2, -1/2\}$  basis. The pulse lengths for the rf1  $\pi$  pulse and rf2  $\pi/2$  pulse were  $1.2 \mu s$  and  $300 \text{ ns}$ , respectively. The rf2 frequency was intentionally detuned by approximately  $200 \text{ kHz}$  from resonance to produce slowly oscillating Ramsey fringes. (b) Ramsey fringe coherence at low field ( $0.3 \text{ mT}$ ) in different bases for the same isopure sample ( $3 \times 10^{18} \text{ cm}^{-2}$ ).  $T_2^* = 1.2 \mu s$  in the  $\{1/2, 3/2\}$  basis (red) and  $13.7 \mu s$  in the  $\{1/2, -1/2\}$  basis (blue). (c)  $T_2^*$  in the  $\{1/2, -1/2\}$  basis (upper) and  $\{1/2, 3/2\}$  basis (lower) for the isopure,  $3 \times 10^{18} \text{ cm}^{-2}$  sample after annealing for  $2 \text{ h}$  at various temperatures. The dashed lines indicate the  $T_2^*$  of the unannealed sample of equal dose in each respective basis. (d) Comparison of  $T_2^*$  of isopure samples versus dose for the two bases. Dots indicate the unannealed samples while stars indicate samples annealed at  $600 \text{ }^\circ\text{C}$  for  $2 \text{ h}$ . Error bars are given to show one standard deviation of the fits in the  $\{1/2, -1/2\}$  basis (the standard deviations in the  $\{1/2, 3/2\}$  basis are smaller than the marker size).

in the dephasing time in the  $\{-1/2, 1/2\}$  basis is also observed after annealing. This improvement may be due to a reduction in strain-induced mixing between the  $|\pm 3/2\rangle$  and  $|\pm 1/2\rangle$  sublevels, which results in states whose energies are not independent of shifts in the ZFS. However, the PL intensity for all samples annealed at temperatures up to  $600 \text{ }^\circ\text{C}$  drops by approximately 30%, while the  $700 \text{ }^\circ\text{C}$  sample PL decreases even further (see Appendix D). This is likely due to vacancies annealing out at higher temperatures or converting to a carbon antisite-vacancy pair [14,38–41]. We measure  $T_2^*$  in both bases for the  $600 \text{ }^\circ\text{C}$  annealed isopure samples and compare with the unannealed samples [Fig. 5(d)]. In particular, the highest observed  $T_2^*$ 's occur in the  $1 \times 10^{17} \text{ cm}^{-2}$  and  $3 \times 10^{17} \text{ cm}^{-2}$  samples, which are  $22\text{--}23 \mu s$  after the  $600 \text{ }^\circ\text{C}$  annealing. The dose dependence in the  $\{1/2, 3/2\}$  basis suggests that the irradiation-induced strain inhomogeneity is still present as a significant decoherence mechanism.

#### IV. OUTLOOK

A number of possibilities remain regarding increasing  $T_2^*$  further, as well as improving other figures of merit of the V2 ensemble as a sensor system. Firstly, the  $^{13}\text{C}$  isotope concentration can be further reduced by an order of magnitude (0.15% versus 0.02%) to levels achieved in other isopure SiC growth [28,31]. Secondly, a low noise external magnetic field larger than what has been used ( $0.3 \text{ mT}$ ) may result in improved coherence times in the  $\{-1/2, 1/2\}$  basis, due to the larger Zeeman splitting suppressing the strain-induced mixing terms. For optimized magnetic sensing, the shot-noise-limited sensitivity scales as  $1/\sqrt{N}$  where  $N$  is the number of emitters, meaning higher V2 densities will result in improved sensitivities. Since there is only a slight dose dependence seen for the highest dephasing times in Fig. 5(d), there appears to be significant room for optimization of the irradiation dose before dipole-dipole interactions between defects significantly affects  $T_2^*$ .

Using the conversion efficiency from related work involving V2 centers created from electron irradiation [39], we roughly estimate the defect densities of our unannealed samples range from approximately  $5 \times 10^{14} \text{ cm}^{-3}$  to approximately  $1 \times 10^{16} \text{ cm}^{-3}$  across the four doses used. We can compare coherence times to isopure diamond samples with comparable NV densities in Bauch *et al.* [8], which are  $6.9 \mu\text{s}$  ( $0.6 \mu\text{s}$ ) in the double quantum basis for NV densities of approximately  $10^{14} \text{ cm}^{-3}$  (approximately  $6 \times 10^{15} \text{ cm}^{-3}$ ). The 4H-SiC samples most closely matching the above NV densities are the unannealed samples with  $1 \times 10^{17} \text{ cm}^{-2}$  and  $3 \times 10^{18} \text{ cm}^{-2}$  electron irradiation, both of which exhibit longer  $T_2^*$ s in the  $\{-1/2, 1/2\}$  basis of  $16.7$  and  $13.7 \mu\text{s}$ , respectively. We expect that this difference results in part from the high density of substitutional nitrogen defects present in diamond samples, a necessary side effect of the low conversion efficiency of NV centers. The use of spin bath driving to suppress decoherence caused by the substitutional nitrogen results in improvements to  $T_2^*$  of  $29.2 \mu\text{s}$  ( $3.4 \mu\text{s}$ ) for the approximately  $10^{14} \text{ cm}^{-3}$  (approximately  $6 \times 10^{15} \text{ cm}^{-3}$ ) NV samples. We also note that a superposition in the double quantum basis accumulates phase twice as quickly, leading to enhanced magnetic sensitivity for schemes utilizing Ramsey interferometry. More recent work with diamond has shown a single quantum basis  $T_2^*$  of  $8.5 \mu\text{s}$  for NVs with a density of approximately  $6 \times 10^{16} \text{ cm}^{-3}$  due to a high conversion efficiency of approximately 28% [42], indicating that substitutional nitrogen is not always a significant limitation.

In summary, we have observed an increase of the inhomogeneous dephasing time of a V2 silicon-vacancy ensemble in 4H-SiC by about a factor of 50 for equivalently electron-irradiated samples. This is a result of systematically suppressing the dominant sources of decoherence, starting with isotopic purification of the sample to decrease the nuclear spin-induced dephasing rate. Strain inhomogeneity-induced dephasing is suppressed via annealing at  $600^\circ\text{C}$  and by choosing a basis insensitive to strain variations. This leads to a  $T_2^*$  longer than  $20 \mu\text{s}$  in the  $\{-1/2, 1/2\}$  basis, with little dependence on irradiation dose. In addition, a maximum Hahn echo decay time of  $105 \mu\text{s}$  was observed for the lowest dose isopure sample, compared with  $4.1 \mu\text{s}$  at low magnetic field for the same dose in a natural abundance sample. These two parameters are critical for quantifying the dc and ac magnetic sensitivities of the spin ensemble. The low optical readout contrast of the V2 center remains a disadvantage for obtaining a high sensitivity, but recent V2 center annealing techniques [14] and demonstrations of cavity-enhanced spin readout of NV centers provide promising paths towards overcoming this limitation [43,44]. These encouraging results motivate further investigation of the V2 ensemble for use in room-temperature quantum systems as an alternative to the NV center in diamond.

## ACKNOWLEDGMENTS

This work was supported by the U.S. Office of Naval Research and the Defense Threat Reduction Agency.

## APPENDIX A: EXPERIMENTAL SETUP

An externally pumped (Coherent Verdi G) continuous-wave Ti:sapphire (Spectra Physics 3900S) laser tuned to 800 nm is used to excite the sample, first passing through a noise eater and then an acousto-optic modulator, which is used to gate the excitation (160-mW cw power). The light is reflected off a dichroic beam splitter, focused via an aspherical lens down onto the face (*c* axis) of the sample with a spot size of approximately  $30 \mu\text{m}$  diameter. The sample is placed in the center of a pair of Helmholtz coils for spatially homogeneous magnetic field generation. rf field excitation of the spin ground state is performed with a rf signal generator (Agilent E8254A) producing an amplitude modulated (900 Hz) signal, gated by an electrical switch to a coaxial cable shorted above the sample surface. The gate of the electrical switch is controlled by a digital delay generator (Stanford DG645). Experiments involving the coherence of the  $\{-1/2, 1/2\}$  basis use an additional pulsed rf source (Stanford SG394), which is combined with the Agilent via an RF splitter (Mini-Circuits ZFRSC-2050) and output to a printed circuit board coplanar waveguide with a 1 mm center conductor instead of the shorted coaxial cable, which produces a more homogeneous rf field across the laser spot. PL is collected back along the same path, transmitted through the dichroic beam splitter, after which an 850-nm long-pass filter further attenuates the laser light. The PL is detected by a silicon photodiode, whose signal is sent into a preamp and then a SR830 DSP lock-in amplifier. The lock-in amplifier measures the amplitude of the signal at the amplitude modulation frequency of the Agilent. All measurements are performed at room temperature.

## APPENDIX B: SAMPLE GROWTH

For both samples, a  $20\text{-}\mu\text{m}$  epilayer of SiC is grown on *n*+ 4H-SiC substrates (II-VI Inc.) oriented  $4^\circ$  off the *c* axis towards the [11–20] crystal axis by hot-wall chemical vapor deposition, with unintentional *p*-type doping levels  $8 \times 10^{14} \text{ cm}^{-3}$  for the isopure sample and  $1 \times 10^{14} \text{ cm}^{-3}$  for the natural abundance sample [45]. Silane ( $\text{SiH}_4$ ) gas is synthesized from  $^{28}\text{Si}$  metal (99.988%) using known procedures [46], modified to improve isolated yield and minimize isotopic contamination. This silane and 99.8% isopure methane is used for the isopure epilayer growth, with a C/Si ratio of 1.65. For the reference SiC, the sample was grown in propane with a C/Si of 1.55. Secondary ion mass spectroscopy data from Evans Analytical Group shows the isotopic concentrations as  $^{13}\text{C} = 0.15\%$  and  $^{29}\text{Si} = 0.01\%$ . The samples are then electron irradiated

with energy 1 MeV at doses varying from  $1 \times 10^{17} \text{ cm}^{-2}$  to  $3 \times 10^{18} \text{ cm}^{-2}$ . Based on previous results with electron-irradiated SiC [39], we estimate our V2 center density to be around  $10^{16} \text{ cm}^{-3}$  for the highest irradiation dose.

### APPENDIX C: SYNTHESIS OF $^{28}\text{SiH}_4$ FROM $^{28}\text{Si}$ METAL

$\text{LiAlH}_4$ , ether, chlorine gas, and tetraglyme were obtained from Aldrich Chemical Company. 99.999% pure aluminum wire was obtained from Alfa. The ether was distilled from sodium benzophenone ketyl and the tetraglyme was distilled under vacuum from sodium-potassium alloy. The  $\text{LiAlH}_4$  was purified by dissolving in an H-tube with dry ether, filtering, and then removing the ether under dynamic vacuum. Purified  $\text{LiAlH}_4$  and dry solvents were stored in an argon-filled drybox. Flexible stainless steel tubing from Swagelock was used for the transfer of gases. The gas cylinder was baked out under vacuum prior to being charged with silane and hydrogen.

#### 1. Synthesis of $^{28}\text{SiCl}_4$

Approximately 7 g of  $^{28}\text{Si}$  was ground to a fine powder using a stainless steel mortar and pestle. The powder was placed in a sample boat formed from Ni foil and placed in an Inconel 625 tube inside a 1 inch diameter tube furnace under flowing argon. The outlet of the reaction tube was connected to a Pyrex U-trap in a Dewar of crushed dry ice, from which the outlet was connected to a bubbler filled with halocarbon oil and vented to the fume hood. Once the tube furnace reached a temperature of  $440^\circ\text{C}$ , chlorine gas from the lecture bottle was bubbled through a halocarbon oil bubbler at a rate of about 5 bubbles/s, and an argon-chlorine mixture was passed over the silicon. The process was continued until the condensate in the U trap was mostly chlorine, as revealed by touching with a liquid nitrogen swab onto the glass, which typically took 3–5 h. Excess chlorine was then allowed to bubble away as the condensate warmed to room temperature, and the product was fractionated on the vacuum line between  $-78^\circ\text{C}$ , ethanol slush, and  $-196^\circ\text{C}$  traps. The  $^{28}\text{SiCl}_4$  still contains residual chlorine, and was dechlorinated by storage for at least several weeks over pure aluminum wire in a Pyrex bulb. Typical isolated yields of  $^{28}\text{SiCl}_4$  were  $>80\%$ .

#### 2. Conversion of $^{28}\text{SiCl}_4$ to $^{28}\text{SiH}_4$

In an argon-filled drybox, about 75 ml of dry tetraglyme, an excess of purified  $\text{LiAlH}_4$  (6.21 g, 163 mmol), and a Teflon covered magnetic stirbar were loaded into a 1500-ml stainless steel cylinder that is rated to 500 psi. On the vacuum line,  $^{28}\text{SiCl}_4$  (20.49 g, 121 mmol) was condensed into the cylinder and the valve closed. The mixture was stirred for several days and then the product was fractionated between a  $-78^\circ\text{C}$  trap and two consecutive  $-196^\circ\text{C}$

TABLE I. PL signal, max ODMR signal, and contrast of annealed samples.

Temperature	PL	Max Rabi (duty cycle corrected)	Max contrast
Nonannealed	518 mV	1.39 mV	0.27%
300 °C	400 mV	1.07 mV	0.27%
400 °C	430 mV	1.25 mV	0.29%
500 °C	376 mV	1.06 mV	0.28%
600 °C	370 mV	1.24 mV	0.33%
700 °C	170 mV	.753 mV	0.44%

traps under dynamic vacuum. The silane in the  $-196^\circ\text{C}$  traps was then condensed into a storage vessel. When sufficient silane has accumulated from repeated reactions, the stored silane was expanded into a gas cylinder and then overpressurized with sufficient high purity  $\text{H}_2$  to produce a 2% mixture. The isotopic purity of the silane was measured using nuclear magnetic resonance, giving a residual concentration of  $^{29}\text{Si}$  of  $<0.004\%$ .

### APPENDIX D: DECREASED PL AND ODMR SIGNAL AT DIFFERENT ANNEALING TEMPERATURES

The highest dose samples ( $3 \times 10^{18} \text{ cm}^{-2}$ ), which have been annealed at temperatures ranging from 300 to  $700^\circ\text{C}$  for 2 h, are measured for their PL brightness and ODMR signal in Table I. The maximum of the first peak of a Rabi oscillation (corrected by the duty cycle of the pulse sequence) is used to characterize the maximum possible ODMR contrast.

- [1] T. Ruster, C. T. Schmiegelow, H. Kaufmann, C. Warschburger, F. Schmidt-Kaler, and U. G. Poschinger, A long-lived Zeeman trapped-ion qubit, *Appl. Phys. B* **122**, 254 (2016).
- [2] M. M. Boyd, T. Zelevinsky, A. D. Ludlow, S. M. Foreman, S. Blatt, T. Ido, and J. Ye, Optical atomic coherence at the 1-second time scale, *Science* **314**, 1430 (2006).
- [3] J. R. Maze, P. L. Stanwix, J. S. Hodges, S. Hong, J. M. Taylor, P. Cappellaro, L. Jiang, M. V. G. Dutt, E. Togan, A. S. Zibrov, A. Yacoby, R. L. Walsworth, and M. D. Lukin, Nanoscale magnetic sensing with an individual electronic spin in diamond, *Nature* **455**, 644 (2008).
- [4] M. W. Doherty, N. B. Manson, P. Delaney, F. Jelezko, J. Wrachtrup, and L. C. L. Hollenberg, The nitrogen-vacancy colour centre in diamond, *Phys. Rep.* **528**, 1 (2013).
- [5] F. Casola, T. van der Sar, and A. Yacoby, Probing condensed matter physics with magnetometry based on nitrogen-vacancy centres in diamond, *Nat. Rev. Mater.* **3**, 1 (2018).
- [6] J. F. Barry, M. J. Turner, J. M. Schloss, D. R. Glenn, Y. Song, M. D. Lukin, H. Park, and R. L. Walsworth, Optical

- magnetic detection of single-neuron action potentials using quantum defects in diamond, *PNAS* **113**, 14133 (2016).
- [7] E. Bauch, S. Singh, J. Lee, C. A. Hart, J. M. Schloss, M. J. Turner, J. F. Barry, L. M. Pham, N. Bar-Gill, S. F. Yelin, and R. L. Walsworth, Decoherence of ensembles of nitrogen-vacancy centers in diamond, *Phys. Rev. B* **102**, 134210 (2020).
- [8] E. Bauch, C. A. Hart, J. M. Schloss, M. J. Turner, J. F. Barry, P. Kehayias, S. Singh, and R. L. Walsworth, Ultra-long Dephasing Times in Solid-State Spin Ensembles via Quantum Control, *Phys. Rev. X* **8**, 031025 (2018).
- [9] L. C. Bassett, A. Alkauskas, A. L. Exarhos, and K.-M. C. Fu, Quantum defects by design, *Nanophotonics* **8**, 1867 (2019).
- [10] D. Simin, F. Fuchs, H. Kraus, A. Sperlich, P. G. Baranov, G. V. Astakhov, and V. Dyakonov, High-Precision Angle-Resolved Magnetometry with Uniaxial Quantum Centers in Silicon Carbide, *Phys. Rev. Appl.* **4**, 014009 (2015).
- [11] H. Kraus, V. A. Soltamov, F. Fuchs, D. Simin, A. Sperlich, P. G. Baranov, G. V. Astakhov, and V. Dyakonov, Magnetic field and temperature sensing with atomic-scale spin defects in silicon carbide, *Sci. Rep.* **4**, 5303 (2014).
- [12] M. Niethammer, M. Widmann, S.-Y. Lee, P. Stenberg, O. Kordina, T. Ohshima, N. T. Son, E. Janzén, and J. Wrachtrup, Vector Magnetometry Using Silicon Vacancies in 4H-SiC Under Ambient Conditions, *Phys. Rev. Appl.* **6**, 034001 (2016).
- [13] S.-Y. Lee, M. Niethammer, and J. Wrachtrup, Vector magnetometry based on  $S=3/2$  electronic spins, *Phys. Rev. B* **92**, 115201 (2015).
- [14] J. B. S. Abraham, C. Gutgsell, D. Todorovski, S. Sperling, J. E. Epstein, B. S. Tien-Street, T. M. Sweeney, J. J. Wathen, E. A. Pogue, P. G. Brereton, T. M. McQueen, W. Frey, B. D. Clader, and R. Osiander, Nanotesla Magnetometry with the Silicon Vacancy in Silicon Carbide, *Phys. Rev. Appl.* **15**, 064022 (2021).
- [15] Ö. O. Soykal and T. L. Reinecke, Quantum metrology with a single spin-3/2 defect in silicon carbide, *Phys. Rev. B* **95**, 081405 (2017).
- [16] D. Simin, V. A. Soltamov, A. V. Poshakinskiy, A. N. Anisimov, R. A. Babunts, D. O. Tolmachev, E. N. Mokhov, M. Trupke, S. A. Tarasenko, A. Sperlich, P. G. Baranov, V. Dyakonov, and G. V. Astakhov, All-Optical Dc Nanotesla Magnetometry Using Silicon Vacancy Fine Structure in Isotopically Purified Silicon Carbide, *Phys. Rev. X* **6**, 031014 (2016).
- [17] P. G. Baranov, A. P. Bundakova, A. A. Soltamova, S. B. Orlinskii, I. V. Borovykh, R. Zondervan, R. Verberk, and J. Schmidt, Silicon vacancy in SiC as a promising quantum system for single-defect and single-photon spectroscopy, *Phys. Rev. B* **83**, 125203 (2011).
- [18] V. A. Soltamov, A. A. Soltamova, P. G. Baranov, and I. I. Proskuryakov, Room Temperature Coherent Spin Alignment of Silicon Vacancies in 4H- and 6H-SiC, *Phys. Rev. Lett.* **108**, 226402 (2012).
- [19] M. Widmann, S.-Y. Lee, T. Rendler, N. T. Son, H. Federer, S. Paik, L.-P. Yang, N. Zhao, S. Yang, I. Booker, A. Denisenko, M. Jamali, S. A. Momenzadeh, I. Gerhardt, T. Ohshima, A. Gali, E. Janzén, and J. Wrachtrup, Coherent control of single spins in silicon carbide at room temperature, *Nat. Mater.* **14**, 164 (2015).
- [20] D. Simin, H. Kraus, A. Sperlich, T. Ohshima, G. V. Astakhov, and V. Dyakonov, Locking of electron spin coherence above 20 Ms in natural silicon carbide, *Phys. Rev. B* **95**, 161201 (2017).
- [21] S. G. Carter, Ö. O. Soykal, P. Dev, S. E. Economou, and E. R. Glaser, Spin coherence and echo modulation of the silicon vacancy in 4H-SiC at room temperature, *Phys. Rev. B* **92**, 161202 (2015).
- [22] I. D. Breev, A. V. Poshakinskiy, V. V. Yakovleva, S. S. Nagalyuk, E. N. Mokhov, R. Hübler, G. V. Astakhov, P. G. Baranov, and A. N. Anisimov, Stress-controlled zero-field spin splitting in silicon carbide, *Appl. Phys. Lett.* **118**, 084003 (2021).
- [23] W. Dong, M. W. Doherty, and S. E. Economou, Spin polarization through intersystem crossing in the silicon vacancy of silicon carbide, *Phys. Rev. B* **99**, 184102 (2019).
- [24] H. B. Banks, Ö. O. Soykal, R. L. Myers-Ward, D. K. Gaskill, T. L. Reinecke, and S. G. Carter, Resonant Optical Spin Initialization and Readout of Single Silicon Vacancies in 4H-SiC, *Phys. Rev. Appl.* **11**, 024013 (2019).
- [25] Ö. O. Soykal, P. Dev, and S. E. Economou, Silicon vacancy center in 4H-SiC: Electronic structure and spin-photon interfaces, *Phys. Rev. B* **93**, 081207 (2016).
- [26] J. S. Embley, J. S. Colton, K. G. Miller, M. A. Morris, M. Meehan, S. L. Crossen, B. D. Weaver, E. R. Glaser, and S. G. Carter, Electron spin coherence of silicon vacancies in proton-irradiated 4H-SiC, *Phys. Rev. B* **95**, 045206 (2017).
- [27] V. A. Soltamov, C. Kasper, A. V. Poshakinskiy, A. N. Anisimov, E. N. Mokhov, A. Sperlich, S. A. Tarasenko, P. G. Baranov, G. V. Astakhov, and V. Dyakonov, Excitation and coherent control of spin qudit modes in silicon carbide at room temperature, *Nat. Commun.* **10**, 1678 (2019).
- [28] R. Nagy, M. Niethammer, M. Widmann, Y.-C. Chen, P. Udvarhelyi, C. Bonato, J. U. Hassan, R. Karhu, I. G. Ivanov, N. T. Son, J. R. Maze, T. Ohshima, Ö. O. Soykal, Á. Gali, S.-Y. Lee, F. Kaiser, and J. Wrachtrup, High-fidelity spin and optical control of single silicon-vacancy centres in silicon carbide, *Nat. Commun.* **10**, 1954 (2019).
- [29] J. F. Barry, J. M. Schloss, E. Bauch, M. J. Turner, C. A. Hart, L. M. Pham, and R. L. Walsworth, Sensitivity optimization for NV-diamond magnetometry, *Rev. Mod. Phys.* **92**, 015004 (2020).
- [30] I. G. Ivanov, M. Yazdanfar, B. Lundqvist, J. T. Chen, J. Hasan, P. Stenberg, R. Liljedahl, N. T. Son, J. W. Ager, O. Kordina, and E. Janzén, High-resolution Raman and luminescence spectroscopy of isotope-pure  $^{28}\text{Si}^{12}\text{C}$ , natural and  $^{13}\text{C}$  – enriched 4H-SiC, *Mater. Sci. Forum* **778–780**, 471 (2014).
- [31] A. Bourassa, C. P. Anderson, K. C. Miao, M. Onizhuk, H. Ma, A. L. Crook, H. Abe, J. Ul-Hassan, T. Ohshima, N. T. Son, G. Galli, and D. D. Awschalom, Entanglement and control of single nuclear spins in isotopically engineered silicon carbide, *Nat. Mater.* **19**, 1319 (2020).
- [32] H. Seo, A. L. Falk, P. V. Klimov, K. C. Miao, G. Galli, and D. D. Awschalom, Quantum decoherence dynamics of divacancy spins in silicon carbide, *Nat. Commun.* **7**, 12935 (2016).
- [33] M. Wagner, N. Q. Thinh, N. T. Son, W. M. Chen, E. Janzén, P. G. Baranov, E. N. Mokhov, C. Hallin, and J. L.

- Lindström, Ligand hyperfine interaction at the neutral silicon vacancy in 4H- and 6H-SiC, *Phys. Rev. B* **66**, 155214 (2002).
- [34] V. V. Dobrovitski, A. E. Feiguin, D. D. Awschalom, and R. Hanson, Decoherence dynamics of a single spin versus spin ensemble, *Phys. Rev. B* **77**, 245212 (2008).
- [35] H. J. Mamin, M. H. Sherwood, M. Kim, C. T. Rettner, K. Ohno, D. D. Awschalom, and D. Rugar, Multipulse Double-Quantum Magnetometry with Near-Surface Nitrogen-Vacancy Centers, *Phys. Rev. Lett.* **113**, 030803 (2014).
- [36] K. Fang, V. M. Acosta, C. Santori, Z. Huang, K. M. Itoh, H. Watanabe, S. Shikata, and R. G. Beausoleil, High-Sensitivity Magnetometry Based on Quantum Beats in Diamond Nitrogen-Vacancy Centers, *Phys. Rev. Lett.* **110**, 130802 (2013).
- [37] C. A. Hart, J. M. Schloss, M. J. Turner, P. J. Scheidegger, E. Bauch, and R. L. Walsworth, N-V-Diamond Magnetic Microscopy Using a Double Quantum 4-Ramsey Protocol, *Phys. Rev. Appl.* **15**, 044020 (2021).
- [38] X. Wang, M. Zhao, H. Bu, H. Zhang, X. He, and A. Wang, Formation and annealing behaviors of qubit centers in 4H-SiC from first principles, *J. Appl. Phys.* **114**, 194305 (2013).
- [39] C. Kasper, D. Klenkert, Z. Shang, D. Simin, A. Gottscholl, A. Sperlich, H. Kraus, C. Schneider, S. Zhou, M. Trupke, W. Kada, T. Ohshima, V. Dyakonov, and G. V. Astakhov, Influence of Irradiation on Defect Spin Coherence in Silicon Carbide, *Phys. Rev. Appl.* **13**, 044054 (2020).
- [40] S. Castelletto, B. C. Johnson, V. Ivády, N. Stavrias, T. Umeda, A. Gali, and T. Ohshima, A silicon carbide room-temperature single-photon source, *Nat. Mater.* **13**, 151 (2014).
- [41] F. Fuchs, V. A. Soltamov, S. Väth, P. G. Baranov, E. N. Mokhov, G. V. Astakhov, and V. Dyakonov, Silicon carbide light-emitting diode as a prospective room temperature source for single photons, *Sci. Rep.* **3**, 1637 (2013).
- [42] C. Zhang, F. Shagieva, M. Widmann, M. Kübler, V. Vorobyov, P. Kapitanova, E. Nenasheva, R. Corkill, O. Rhrle, K. Nakamura, H. Sumiya, S. Onoda, J. Isoya, and J. Wrachtrup, Diamond Magnetometry and Gradiometry Towards Subpicotesla Dc Field Measurement, *Phys. Rev. Appl.* **15**, 064075 (2021).
- [43] E. R. Eisenach, J. F. Barry, M. F. O'Keeffe, J. M. Schloss, M. H. Steinecker, D. R. Englund, and D. A. Braje, Cavity-enhanced microwave readout of a solid-state spin sensor, *Nat. Commun.* **12**, 1357 (2021).
- [44] J. Ebel, T. Joas, M. Schalk, P. Weinbrenner, A. Angerer, J. Majer, and F. Reinhard, Dispersive readout of room-temperature spin qubits, *Quantum Sci. Technol.* **6**, 03LT01 (2021).
- [45] R. L. Myers-Ward, B. L. VanMil, K.-K. Lew, P. B. Klein, E. R. Glaser, J. D. Caldwell, M. A. Mastro, L. Wang, P. Zhao, C. R. Eddy, and D. K. Gaskill, Investigation of deep levels in nitrogen doped 4H-SiC epitaxial layers grown on 4° and 8° off-axis substrates, *J. Appl. Phys.* **108**, 054906 (2010).
- [46] G. Brauer, *Handbook of Preparative Inorganic Chemistry* (Academic Press, New York, NY, 1963), Vol. 1, pp. 679–682.